ACS OMEGA

http://pubs.acs.org/journal/acsodf

Article

Mineralogical and Geochemical Characteristics of Banded Agates from Placer Deposits: Implications for Agate Genesis

Mengmeng Shen, Zhiyun Lu, and Xuemei He*

Cite This: *ACS Omega* 2022, 7, 23858−23864

Read Online

ACCESS | Metrics & More | Article Recommendations | Supporting Information

ABSTRACT: The phase composition and geochemical characteristics in banded agates with different structural sequences have been investigated in detail. The results reveal that the agate bands have a combination of a pseudo-granular silica → fibrous chalcedony → crystalline quartz (type I) sequence and a newly discovered pseudo-granular silica → crystalline quartz (type II) sequence. The banded agates mainly consist of α-quartz, moganite, and a minor amount of amorphous silica, goethite, hematite, kaolinite, illite, and carbonates. With the evolution of two structural sequences, the content of α-quartz and moganite increases and decreases, respectively. There is no moganite in crystalline quartz. The increased concentration of trace elements like Li, Na, Al, K, Ca, Ti, Mn, and Fe in different bands may correspond to the decrease in the water content in the mineral-forming fluid. The increased trace elements promote the structural transformation process of silica. With the evolution of the type I sequence, the thermal gradients between adjacent bands are 17 and 51 °C, respectively. In contrast, a significantly higher thermal gradient of 53−66 °C is exhibited when pseudo-granular silica transforms directly to crystalline quartz. It is inferred that a slightly increased thermal gradient between adjacent bands promotes the structural transformation process of the type I sequence. The sharply increasing thermal gradient between adjacent bands leads to the formation of the type II sequence from pseudo-granular silica to crystalline quartz. The formation process of different structural sequences in agate may be controlled together by trace element concentrations and thermal gradients.

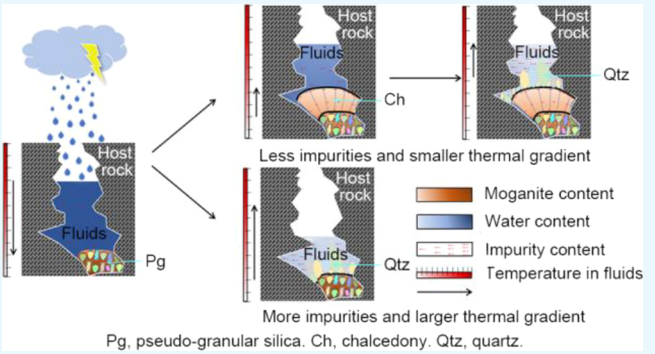

Pg, pseudo-granular silica. Ch, chalcedony. Qtz, quartz.

1. INTRODUCTION

Agate generally refers to the silica aggregate with a banded texture, and outputs as crust and amygdala in the basalt, andesite.[1−4] Agate is mainly composed of fibrous chalcedony, crystalline quartz, and a minor amount of pseudo-granular silica.[5−10] The mineral phases existing in these silicas are mainly α-quartz and moganite. Moganite is the monoclinic silica and usually coexists widely with α-quartz in the pseudo-granular silica and fibrous chalcedony.[11−14] The presence of moganite in agate indicates a lower crystallinity of silicas at the early stages of diagenesis.[15,16] Because of the various formation conditions, there is a significant content difference of moganite (I_{501}/I_{463}) in different bands measured by Raman spectra. The I_{501}/I_{463} value provides information on the crystallinity of silica hydrothermal fluids at different cooling stages.[17,18] Lee (2007) found that the completely crystallized agate in a period hydrothermal fluid showed the growth sequence of amorphous silica + microcrystalline quartz → fibrous chalcedony → crystalline quartz.[19] This crystalline sequence of silica is accompanied by an increase in the SiO_2 crystallinity and a decrease in the water content.[19] In addition, the structural evolution of silica may also be accompanied by the systematic changes in the content of Al and Fe.[20,21] However, the distribution of trace element concentrations and formation temperatures in different bands are still lacking. In this study, two banded agates from Xunke, Heilongjiang, China, were mineralogically and geochemically investigated to obtain information on the spatial change of trace element concentrations and formation temperatures in different bands. This work aims to determine the controlling factors during the formation process of different structural sequences in agate and provide support for exploring the origin of banded agate.

2. MATERIALS AND METHODS

Two agate samples with rich bands from the secondary placer deposits in Xunke, Heilongjiang, China, were selected as the research objects and numbered BH01 and BH02, respectively (Figure 1).

Received: April 23, 2022
Accepted: June 22, 2022
Published: June 30, 2022

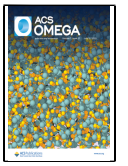

Figure 1. Agates with rich bands from Heilongjiang Province, China.

The banded agates were cut into thin sections along the cross section to observe the structural characteristics and mineral composition with an Olympus BX-51 polarizing microscope. The thin sections were etched in 45% hydrofluoric (HF) acid for 60 s at room temperature. High-resolution secondary electron (SEM) images and backscattered electron (BSE) images were acquired using a scanning electron microscope (FEI Nova NanoSEM 450) at conditions of 5.00−7.00 kV, 140 pA and a working distance of 12.4−933.0 μm.

Raman spectra and Raman mappings of banded agates were measured with a HORIBA HR-Evolution Raman spectrometer equipped with a 532 nm solid stage laser at a 50 times magnification. The Raman spectra were recorded at a range of 100−1100 cm^{-1} and resolution 1 cm^{-1}.

The elemental maps of banded agates were measured using a Bruker Micro-XRF spectrometer (M4 TORNADO). The spectrometer was equipped with an X-ray tube (Rh anode) with a polycapillary X-ray optic. The system worked at 50 kV and 600 μA, with chambering at air 20 mbar and an acquisition time of 10 ms per pixel. The data were processed by the mineral analyzer software for M4 TORNADO.

The trace element data of banded agates was acquired with a laser ablation inductively coupled plasma mass spectroscopy (LA-ICP-MS) at the Laboratory of Elemental Geochemistry, Institute of Science, China University of Geosciences, Beijing. The power of the mass spectrometer was set to 1550 W, and the laser system was operated at a wavelength of 193 nm and a laser spot diameter of 50 μm. The accredited standard NIST 610 was used for calibration procedures, with Si as an internal standard.[22] The relative error of the LA-ICP-MS test is 3%.

The oxygen isotope ratios of different bands were measured using a Delta v main gas isotope mass spectrometer. The samples were heated with a 20 W CO_2 laser, with BrF_5 as the fluorinating agent. The released oxygen was converted to CO_2 and then admitted on-line to the mass spectrometer. The precision of the method is ±0.1 ‰ for less than 100 μg samples, and the temperature relative error calculated according to the error transfer formula is ±2.0%.[23]

3. RESULTS

3.1. Microstructure Characteristics. The agate samples mainly consist of the following three different structures of silica under cross-polarized light (CPL) (Figure 2). (1) Pseudo-granular silica, showing a twisted extinction under CPL and with random mutual orientation of the individual grains.[24,25] (2) Fibrous chalcedony, characterized by its negative optical character of elongation and growth perpendicular to pseudo-granular silica boundaries.[26] (3) Crystalline quartz, growing in roughly the same direction as chalcedony.[10] The BH01-1 region presents the structural sequence of pseudo-granular silica → fibrous chalcedony → crystalline quartz (type I) (Figure 2a, b). Besides, a new structural sequence of direct transformation from pseudo-granular silica to crystalline quartz (type II) was found in regions BH01-2 and BH02-1 (Figure 2c−f).

Figures 3 and S1 show the SEM and BSE images of different structural sequences in banded agates, respectively. After being etched by HF, dense alternating units with a constant length but different etching depths were found at the boundary of different bands. The relative deep and shallow etching bands correspond to the high and low contents of (OH) (Figure 3a−c).[27−30] These oscillating bands reflect drastic changes in the content of water and trace elements such as Al and Fe, as well as the crystallinity changes during different structural transitions. Pseudo-granular silica is mainly composed of a central crystalline core and an outer layer of amorphous silica. The core can be microcrystalline quartz or microcrystalline opal with a diameter of 20 μm (Figure 3d−f).

3.2. Raman Spectra. The Raman spectra collected on the banded agates are shown in Figure 4. Both spectra show characteristic peaks of quartz at 126 and 465 cm^{-1}. They are related to the rotational or translational vibrations of [SiO4] and the symmetric stretching−bending vibration of Si−O−Si, respectively.[11,31] In addition, spectrum b exhibits a peak at 808 cm^{-1} caused by the symmetric stretching vibration of Si−O−Si in quartz.[32] In both spectra, the presence of goethite is confirmed by peaks at 205, 240, 300, and 403 cm^{-1}, while the

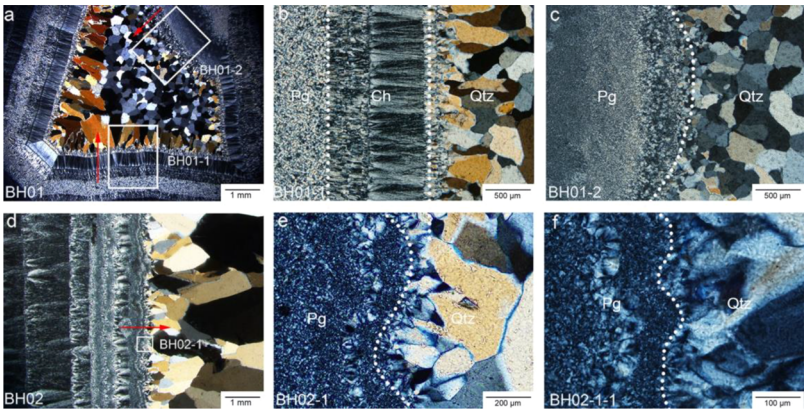

Figure 2. Microstructure characteristics of agate samples BH01 and BH02 observed under CPL. (a) Agate BH01 with two different structural sequences. (b) Enlarged view of the type I sequence in region BH01-1. (c) Enlarge view of the type II sequence in region BH01-2. (d) Agate BH02 shows the type II sequence. (e, f) Enlarged view of region BH02-1 in Figure 2d. The red arrow indicates the growth direction of banded agates. Pg, pseudo-granular silica. Ch, chalcedony. Qtz, quartz.

https://doi.org/10.1021/acsomega.2c02538
ACS Omega 2022, 7, 23858−23864

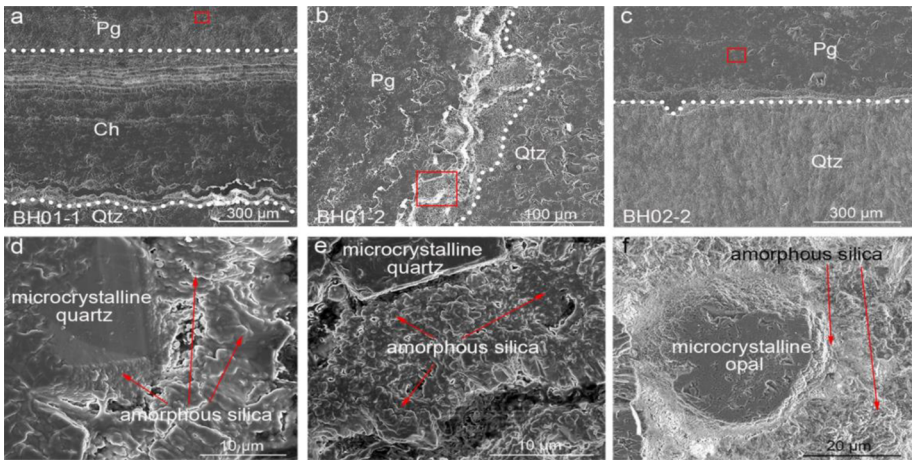

Figure 3. Microstructure characteristics of banded agates observed under SEM after HF etching. (a) Type I sequence with dense alternating units at the boundary of different bands in region BH01-1. (b, c) Type II sequence with dense alternating units at the boundary of different bands in regions BH01-2 and BH02-2. (d, e) Enlarged view of the pseudo-granular structure in Figure 3a, b with a microcrystalline opal core surrounded by radially arranged amorphous silica. (f) Enlarged view of the pseudo-granular structure in Figure 3c with a microcrystalline opal core surrounded by radially arranged amorphous silica.

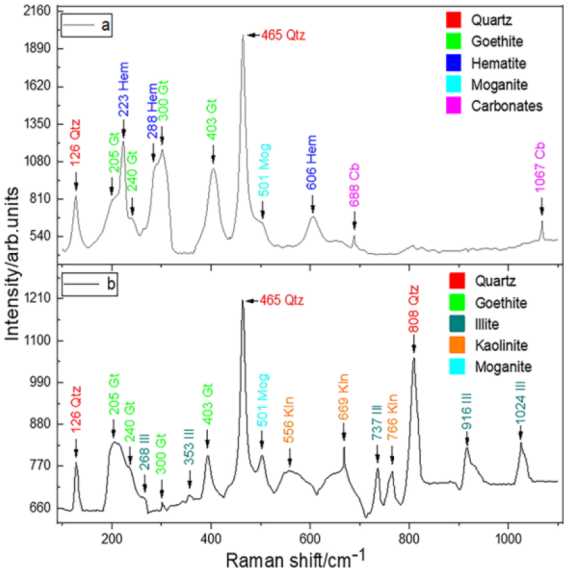

Figure 4. Raman spectra of agate samples BH01 (a) and BH02 (b) and their peak assignments. Gt, Goethite. Hem, Hematite. Mog, Moganite. Cb, Carbonates. Ill, illite. Kln, Kaolinite.

peak at 501 cm^{-1} is attributed to moganite.[33−35] In spectrum a, the presence of hematite is confirmed by peaks at 223, 288, and 606 cm^{-1}, and weak carbonate features are observed at 688 and 1067 cm^{-1}.[36,37] In spectrum b, the vibrational peaks of Si−O−Si and [SiO4] are observed at 268, 353, 916, and 1024 cm^{-1}, while the vibrational peak of Al−O appears at 737 cm^{-1}, and these peaks are characteristic of illite.[38] Spectrum b also shows peaks at 556, 669, and 766 cm^{-1}. They are assigned to the bending vibration of Si−O bonds, the bending vibration of Al−OH bonds, and the disorder between the TO layers in kaolinite, respectively.[39]

The phase distribution patterns in different structural sequences of banded agates are obtained from the Raman intensity mapping of α-quartz (465 cm^{-1}) and moganite (501 cm^{-1}).[40] The results in Figure 5 show that α-quartz is distributed in pseudo-granular silica as islands, corresponding to the microcrystalline quartz core observed under SEM

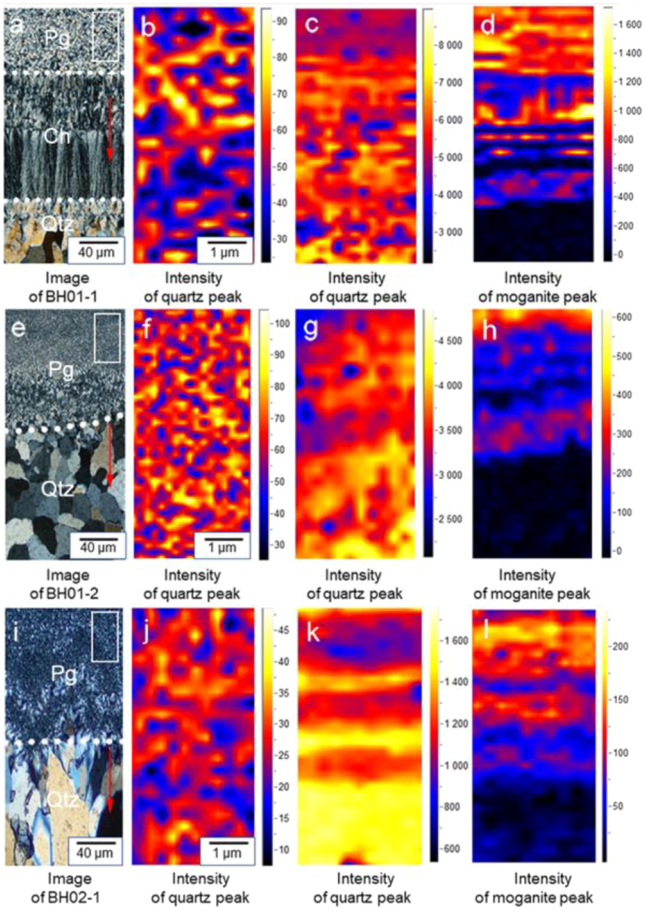

Figure 5. Distribution of α-quartz and moganite in two different structural sequences of banded agates by Raman mappings. (a, e, i) Type I and type II sequences of banded agates under CPL. (b, f, j) Distribution of quartz at the white rectangle region shown in Figure 4a, e, i. (c, g, k) Quartz distribution images in BH01-1, BH01-2, and BH02-1 regions. (d, h, l) Distribution of moganite in BH01-1, BH01-2, and BH02-1 regions. The red arrow indicates the growth direction of banded agates.

https://doi.org/10.1021/acsomega.2c02538
ACS Omega 2022, 7, 23858−23864

(Figure 5b, f, j). With the evolution of the structural sequence of the agate samples, there is an increase in the α-quartz content and a reduction in the moganite content, and moganite is substantially absent in crystalline quartz (Figure 5c, d, g, h, k, l). In addition, the changes in the content of α-quartz and moganite are both oscillatory processes (Figure 5c, d, g, h, k, l).

3.3. Elemental Mapping by μ-XRF. To obtain the chemical composition difference in different bands, μ-XRF mappings were performed on different structural sequences of banded agate, and the results are shown in Figure 6. The

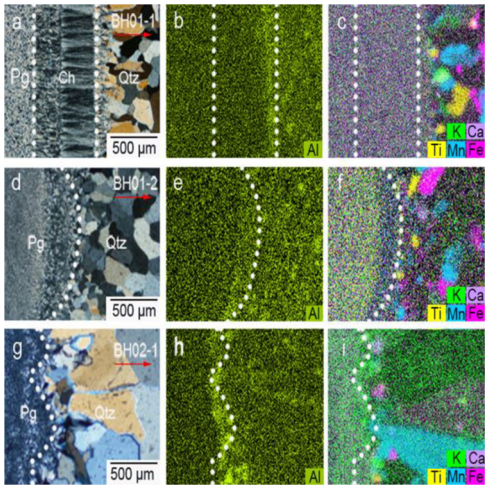

Figure 6. Elemental distribution maps produced by μ-XRF mapping on different structural sequences of banded agates. (a, d, g) Type I and type II sequences of banded agates under CPL. (b, e, h) Distribution images of Al in BH01-1, BH01-2, and BH02-1 regions. (c, f, i) Distribution images of K, Ca, Ti, Mn, and Fe in BH01-1, BH01-2, and BH02-1 regions. Red arrow shows the growth direction of banded agates.

distribution of Al, K, Ca, Ti, Mn, and Fe is relatively uniform in pseudo-granular silica and chalcedony (Figure 6). It is noticed that the Al content in crystalline quartz is significantly higher than that in pseudo-granular silica and fibrous chalcedony, and the Al content increases sharply at the beginning crystalline quartz (Figure 6b, e, h). Quartz grains enriched with K, Ca, Ti, Mn, and Fe are not completely consistent, indicating that they exhibit distinct differentiation and exclusive features in quartz (Figure 6c, f, i).

3.4. Trace Element Contents. Figure 7 and Table S1 show the statistical content and detailed data of trace elements collected on pseudo-granular silica, fibrous chalcedony, and crystalline quartz. The content of Li, Na, Al, K, Ca, Ti, Mn, and Fe all increases with the evolution of two structural sequences (Figure 7). In addition, the increased process of the trace elements content in the type II sequence (BH01-2 and BH02-1) is more significant than that in the type I sequence (BH01-1).

3.5. Equilibrium Formation Temperature. The equilibrium formation temperature and the composition of mineral-forming fluids at different bands of type I and II sequences were measured by the oxygen isotope ratios (Table 1). Combined with the $\delta^{18}O$ value and the homogenization temperature (T_{hom}) data, the oxygen isotopic composition in the mineral-forming fluid ($\delta^{18}O_{H2O}$) is calculated to be between −7.9 and +3.0‰, indicating that meteoric water

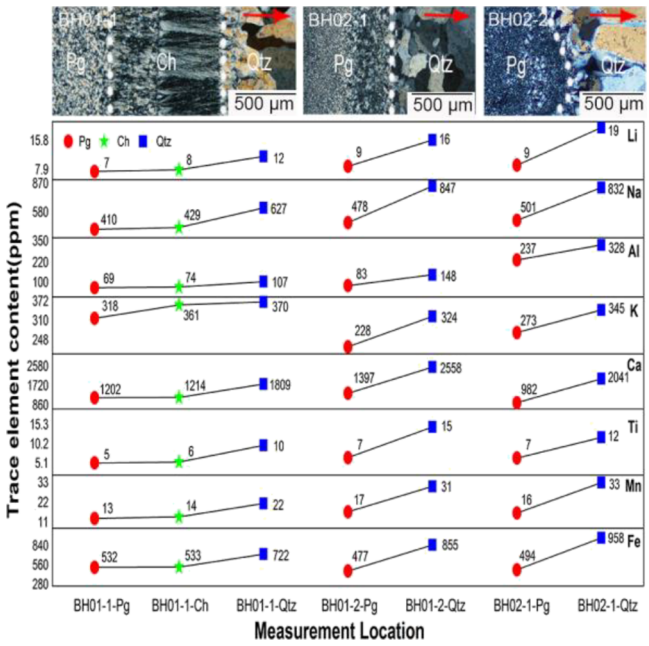

Figure 7. Concentration of trace elements recorded at different bands of type I and type II sequences. The red arrow indicates the growth direction of banded agates.

Table 1. Oxygen Isotope Data and Calculated Equilibrium Temperature of Different Bands in Agate Samples

sample	$\delta^{18}O_{SMOW}$ (‰)	T_{hom} (°C)	$\delta^{18}O_{H2O}$ (‰)	T_{met} (°C)	T_{oc} (°C)	T_{mag} (°C)
BH01-1-Pg	+16.7	130–170	−0.5 ~ +3.0	60	135	254
BH01-1-Ch	+15.2	130–170	−2.0 ~ +1.5	69	152	291
BH01-1-Qtz	+11.4	120–170	−6.9 ~ −2.3	95	203	432
BH01-2-Pg	+16.5	130–170	−0.7 ~ +2.8	62	137	259
BH01-2-Qtz	+11.4	120–170	−6.9 ~ −2.3	95	203	432
BH02-1-Pg	+13.9	130–170	−3.3 ~ +0.2	77	167	329
BH02-1-Qtz	+10.4	120–170	−7.9 ~ −3.3	102	220	492

exists in the mineral-forming fluid (Table 1).[41−44] The temperatures were calculated according to the equation $\delta^{18}O = 1000\ln\alpha_{QW} = 3.34(10^6\ T^{-2}) - 3.31$ for equilibrium isotope exchange with meteoric water (−10‰ = T_{met}), oceanic water (±0‰ = T_{oc}), and magmatic water (+8‰ = T_{mag}), in which α_{QW} is the O-isotope fractionation factor between quartz and water, and T is expressed in degrees K (Table 1).[45,46] The results in Table 1 illustrate that the calculations for pure magmatic water lead to isotopic equilibrium temperatures as high as 492 °C, and the result seems to be unlikely (Table 1). According to the range of $\delta^{18}O_{H2O}$, it is inferred that the mineral-forming fluid of banded agates is a mixture of magmatic water and meteoric water, so the isotopic equilibrium temperature with seawater is selected as the formation temperature of the agate band.[47−49] Based on the previous calculation results, it can be concluded that the formation temperature of agate samples ranges from 135 to 220 °C (Figure 8).[50−52] Therefore, with the structural sequence evolution of pseudo-granular silica → fibrous

https://doi.org/10.1021/acsomega.2c02538
ACS Omega 2022, 7, 23858−23864

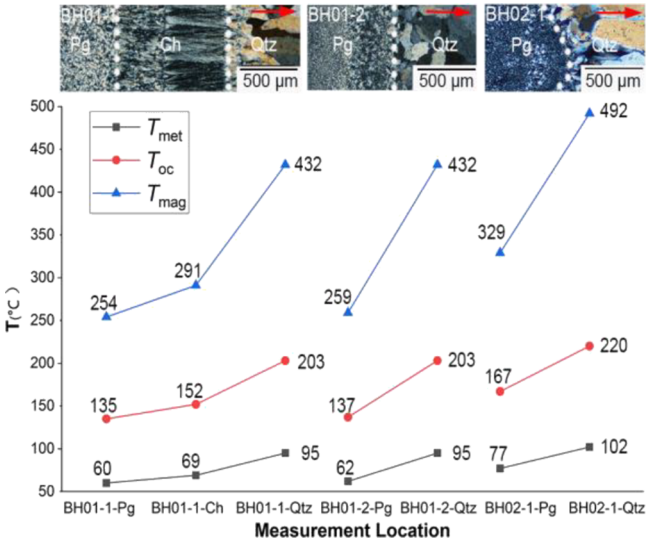

Figure 8. Equilibrium formation temperature at different bands of type I and II sequences in banded agates. The red arrow indicates the growth direction of banded agates.

chalcedony → crystalline quartz, the formation temperature of different bands increases from 135 to 152 °C and then to 203 °C, and the thermal gradients of adjacent bands are 17 and 51 °C, respectively (Figure 8). When directly transforming from pseudo-granular silica to crystalline quartz, the corresponding formation temperature increases from 137−167 to 203−220 °C, and the thermal gradient of adjacent bands is as high as 53−66 °C. The thermal gradient in the type II sequence is significantly higher than that in the type I sequence (Figure 8).

4. DISCUSSION

4.1. Effects of Trace Elements on the Silica Structural Transformation Rate. Previous studies have shown that variations of silica concentration and saturation in mineral-forming fluid during agate formation correspond to the oscillatory changes of α-quartz and moganite contents and may have different effects on the structural transition of silica.[53−56] Besides, the impurity absorption effect by goethite, kaolinite, illite, and carbonates reduces the silica concentration in the mineral-forming fluid and promotes the structure transformation process of silica.[57−59] The sharp increase in the Al content at the beginning crystalline quartz supports the dissolution−reprecipitation mechanism of silica.[60] In our work, with the evolution of two structural sequences, trace element concentrations such as Li, Na, Al, K, Ca, Ti, Mn, and Fe were also found to increase gradually. This phenomenon may correspond to the decrease in the water content in the mineral-forming fluid.[19,61] In addition, the increased process of the trace element content in the type II sequence (BH01-2 and BH02-1) is more significant than that in the type I sequence (BH01-1). It is inferred that the increased trace elements promote the silica structural transformation rate. Among them, a minor amount of Al catalyzes the structural transformation process of silica.[62]

4.2. Effects of Formation Temperature on the Silica Structural Transformation Pathway. With the evolution of the type I sequence, the thermal gradients between adjacent bands are 17 and 51 °C, respectively. In contrast, a significantly higher thermal gradient of 53−66 °C exhibits when pseudo-granular silica transforms directly to crystalline quartz. Different thermal gradients between adjacent bands produce various effects on the structural transformation process of silica. The slightly increased thermal gradient between adjacent bands reduces the relative supersaturation in the mineral-forming fluid and promotes the structural transformation process of the type I sequence.[59,63] Notably, the sharply increasing thermal gradient between adjacent bands leads to a significant decrease in relative supersaturation in the mineral-forming fluid suitable for precipitating crystalline quartz from the monomer solution. Therefore, the type II sequence can be formed by bypassing fibrous chalcedony.

5. CONCLUSIONS

The pseudo-granular silica → fibrous chalcedony → crystalline quartz (type I) sequence and the newly discovered pseudo-granular silica → crystalline quartz (type II) sequence are widely found in agates from Xunke, Heilongjiang, China, indicating that the mineral-forming fluid may exhibit multiple changing patterns during crystallization. In this study, the phase composition of agate and the content difference of α-quartz and moganite in different structural sequences were systematically studied. Compared with sequence I, sequence II shows a more significant increase in the trace element concentration and temperature gradient. This difference can provide evidence for studying the influencing factors of silica structure evolution.

■ ASSOCIATED CONTENT

Supporting Information

The Supporting Information is available free of charge at https://pubs.acs.org/doi/10.1021/acsomega.2c02538.

Figure S1. Microstructure characteristics of banded agates observed under BSE after HF etching; Table S1. Concentrations (in ppm) of the investigated trace elements in the different bands (PDF)

■ AUTHOR INFORMATION

Corresponding Author

Xuemei He − *School of Gemmology, China University of Geosciences, Beijing 100083, China;* orcid.org/0000-0002-5758-4057; Email: Hexuemei3127@126.com

Authors

Mengmeng Shen − *School of Gemmology, China University of Geosciences, Beijing 100083, China;* orcid.org/0000-0001-7688-6993

Zhiyun Lu − *School of Earth Sciences, Zhejiang University, Hangzhou 310027, P. R. China*

Complete contact information is available at: https://pubs.acs.org/10.1021/acsomega.2c02538

Author Contributions

X.H. participated in the design and coordination of the study. M.S. and Z.L. drafted the manuscript, took all the photographs, and created the TOC graphic in the manuscript. All authors have given approval to the final version of the manuscript.

Funding

This research was funded by the project of "Geology of mineral resources in China" from China Geological Survey (Grant No. DD20160346, DD20190379) and the project of "Beihong Agate" from China National Standardizing Committee (Grant No. 20161367-T-334).

Notes

The authors declare no competing financial interest.

■ ACKNOWLEDGMENTS

The authors thank the Laboratory of the Jewelry College, China University of Geosciences, Beijing, for their support. The authors also thank two reviewers for their valuable suggestions.

■ REFERENCES

(1) Moxon, T.; Ríos, S. Moganite and water content as a function of age in agate: an XRD and thermogravimetric study. *Eur. J. Mineral.* **2004**, *16*, 269−278.
(2) Götze, J.; Nasdala, L.; Kempe, U.; Libowitzky, E.; Rericha, A.; Vennemann, T. The origin of black colouration in onyx agate from Mali. *Mineral. Mag.* **2012**, *76*, 115−127.
(3) Götze, J.; Gaft, M.; Möckel, R. Uranium and uranyl luminescence in agate/chalcedony. *Mineral. Mag.* **2015**, *79*, 985−995.
(4) Schmidt, P.; Frohlich, F. Temperature dependent crystallographic transformations in chalcedony, SiO_2, assessed in mid infrared spectroscopy. *Spectrochim. Acta, Part A* **2011**, *78*, 1476−1481.
(5) French, M. W.; Worden, R. H.; Lee, D. R. Electron backscatter diffraction investigation of length-fast chalcedony in agate: implications for agate genesis and growth mechanisms. *Geofluids* **2013**, *13*, 32−44.
(6) Natkaniec-Nowak, L.; Dumańska-Słowik, M.; Gaweł, A.; Łatkiewicz, A.; Kowalczyk-Szpyt, J.; Wolska, A.; Milovská, S.; Luptáková, J.; Ładoń, K. Fire agate from the Deer Creek deposit (Arizona, USA) - new insights into structure and mineralogy. *Mineral. Mag.* **2020**, *84*, 343−354.
(7) Svetova, E. N.; Chazhengina, S. Y.; Stepanova, A. V.; Svetov, S. A. Black Agates from Paleoproterozoic Pillow Lavas (Onega Basin, Karelian Craton, NW Russia): Mineralogy and Proposed Origin. *Minerals* **2021**, *11*, 918.
(8) Flörke, O. W.; Köhler-Herbertz, B.; Langer, K.; Tönges, I. Water in microcrystalline quartz of volcanic origin: agates. *Contrib. Mineral. Petrol.* **1982**, *80*, 324−333.
(9) Schmidt, P.; Bellot-Gurlet, L.; Leá, V.; Sciau, P. Moganite detection in silica rocks using Raman and infrared spectroscopy. *Eur. J. Mineral.* **2013**, *25*, 797−805.
(10) Hatipoğlu, M.; Ajò, D.; Sezai-Kırıkoğlu, M. Cathodoluminescence (CL) features of the Anatolian agates, hydrothermally deposited in different volcanic hosts from Turkey. *J. Lumin.* **2011**, *131*, 1131−1139.
(11) Dumańska-Słowik, M.; Natkaniec-Nowak, L.; Wesełucha-Birczyńska, A.; Gaweł, A.; Lankosz, M.; Wröbel, P. Agates from Sidi Rahal, in the Atlas Mountains of Morocco: Gemological Characteristics and Proposed Origin. *Gems Gemol.* **2013**, *49*, 148−159.
(12) Pršek, J.; Dumańska-Słowik, M.; Powolny, T.; Natkaniec-Nowak, L.; Toboła, T.; Zych, D.; Skrepnicka, D. Agates from Western Atlas (Morocco)-Constraints from Mineralogical and Microtextural Characteristics. *Minerals* **2020**, *10*, 198.
(13) Schmidt, P.; Bellot-Gurlet, L.; Slodczyk, A.; Fröhlich, F. A hitherto unrecognised band in the Raman spectra of silica rocks: influence of hydroxylated Si-O bonds (silanole) on the Raman moganite band in chalcedony and flint (SiO_2). *Phys. Chem. Minerals* **2012**, *39*, 455−464.
(14) Preusser, F.; Chithambo, M. L.; Götte, T.; Martini, M.; Ramseyer, K.; Sendezera, E. J.; Susino, G. J.; Wintle, A. G. Quartz as a natural luminescence dosimeter. *Earth-Sci. Rev.* **2009**, *97*, 184−214.
(15) Zhang, M.; Moxon, T. Infrared absorption spectroscopy of SiO_2-moganite. *Am. Mineral.* **2014**, *99*, 671−680.
(16) Rodgers, K. A.; Hampton, W. A. Laser Raman identification of silica phases comprising microtextural components of sinters. *Mineral. Mag.* **2013**, *67*, 1−13.
(17) Götze, J.; Nasdala, L.; Kleeberg, R.; Wenzel, M. Occurrence and distribution of "moganite" in agate/chalcedony: a combined micro-Raman, Rietveld, and cathodoluminescence study. *Contrib. Mineral. Petrol.* **1998**, *133*, 96−105.
(18) Nash, D. J.; Hopkinson, L. A reconnaissance laser Raman and Fourier transform infrared survey of silcretes from the Kalahari Desert, Botswana. *Earth Surf. Processes Landforms* **2004**, *29*, 1541−1558.
(19) Lee, D. R. Characterisation of silica minerals in a banded agate: implications for agate genesis and growth mechanisms. *Masters Res.* **2007**, 1−18.
(20) Stoch, L.; Łaczka, M.; Wacławska, I. DTA and X-ray diffraction study of the phase transformation of silica minerals. *Thermochim. Acta* **1985**, *93*, 533−536.
(21) Chakraborty, D.; Lehmann, G. Distribution of OH in synthetic and natural quartz crystals. *J. Solid State Chem.* **1976**, *17*, 305−311.
(22) Hollocher, K.; Ruiz, J. Major and trace element determinations on NIST glass standard reference materials 611, 612, 614 and 1834 by inductively coupled plasma-mass spectrometry. *Geostand. Newsl.* **1995**, *19*, 27−34.
(23) Vennemann, T. W.; Morlok, A.; Engelhardt, W. V.; Kyser, K. Stable isotope composition of impact glasses from the Nördlinger Ries impact crater, Germany. *Geochim. Cosmochim. Acta* **2001**, *65*, 1325−1336.
(24) Zhang, X.; Ji, L.; He, X. Gemological Characteristics and Origin of the Zhanguohong Agate from Beipiao, Liaoning Province, China: A Combined Microscopic, X-ray Diffraction, and Raman Spectroscopic Study. *Minerals* **2020**, *10*, 401.
(25) Dong, G.; Morrison, G.; Jaireth, S. Quartz textures in epithermal veins, Queensland; classification, origin and implication. *Econ. Geol.* **1995**, *90*, 1841−1856.
(26) Commin-Fischer, A.; Berger, G.; Polvé, M.; Dubois, M.; Sardini, P.; Beaufort, D.; Formoso, M. Petrography and chemistry of SiO_2 filling phases in the amethyst geodes from the Serra Geral Formation deposit, Rio Grande do Sul, Brazil. *J. South Am. Earth Sci.* **2010**, *29*, 751−760.
(27) Frondel, C. Systematic compositional zoning in the quartz fibers of agates. *Am. Mineral.* **1985**, *70*, 975−979.
(28) Moxon, T.; Palyanova, G. Agate Genesis: A Continuing Enigma. *Minerals* **2020**, *10*, 953.
(29) Moxon, T.; Petrone, C. M.; Reed, S. J. B. Characterization and genesis of horizontal banding in Brazilian agate: an X-ray diffraction, thermogravimetric and electron microprobe study. *Mineral. Mag.* **2013**, *77*, 227−248.
(30) Heaney, P. J. A proposed mechanism for the growth of chalcedony. *Contrib. Mineral. Petrol.* **1993**, *115*, 66−74.
(31) Mercury, L.; de Bilbao, E.; Simon, P.; Raimbourg, H.; Bergonzi, I.; Hulin, C.; Canizarès, A.; Shmulovich, K. I. Quartz Stressing and Fracturing by Pore Pressure Dropping Down to Negative Pressure. *ACS Earth Space Chem.* **2021**, *5*, 170−185.
(32) Dračínský, M.; Benda, L.; Bouř, P. Ab initio modeling of fused silica, crystal quartz, and water Raman spectra. *Chem. Phys. Lett.* **2011**, *512*, 54−59.
(33) Harris, C. Oxygen-isotope zonation of agates from Karoo volcanics of the Skeleton Coast, Namibia. *Am. Mineral.* **1989**, *74*, 476−481.
(34) Dumańska-Słowik, M.; Powolny, T.; Sikorska-Jaworowska, M.; Gaweł, A.; Kogut, L.; Poloński, K. Characteristics and origin of agates from Płoczki Gorne (Lower Silesia, Poland): A combined microscopic, micro-Raman, and cathodoluminescence study. *Spectrochim. Acta, Part A* **2018**, *192*, 6−15.
(35) Heaney, P. J.; McKeown, D. A.; Post, J. E. Anomalous behavior at the I12/a to Imab phase transition in SiO_2-moganite: An analysis using hard-mode Raman spectroscopy. *Am. Mineral.* **2007**, *92*, 631−639.
(36) Legodi, M. A.; de Waal, D. The preparation of magnetite, goethite, hematite and maghemite of pigment quality from mill scale iron waste. *Dyes Pigm.* **2007**, *74*, 161−168.
(37) Gunasekaran, S.; Anbalagan, G.; Pandi, S. Raman and infrared spectra of carbonates of calcite structure. *J. Raman Spectrosc.* **2006**, *37*, 892−899.

https://doi.org/10.1021/acsomega.2c02538
ACS Omega 2022, 7, 23858−23864

(38) Liu, W. Modeling description and spectroscopic evidence of surface acid-base properties of natural illites. *Water Res.* **2001**, *35*, 4111−4125.
(39) Legodi, M. A.; de Waal, D. Raman spectroscopic study of ancient South African domestic clay pottery. *Spectrochim. Acta, Part A* **2007**, *66*, 135−142.
(40) Götze, J.; Stanek, K.; Orozco, G.; Liesegang, M.; Mohr-Westheide, T. Occurrence and Distribution of Moganite and Opal-CT in Agates from Paleocene/Eocene Tuffs, El Picado (Cuba). *Minerals* **2021**, *11*, 531.
(41) Li, J.; Hu, R.; Xiao, J.; Zhuo, Y.; Yan, J.; Oyebamiji, A. Genesis of gold and antimony deposits in the Youjiang metallogenic province, SW China: Evidence from in situ oxygen isotopic and trace element compositions of quartz. *Ore Geol. Rev.* **2020**, *116*, No. 103257.
(42) Lubben, J. D.; Cline, J. S.; Barker, S. L. L. Ore fluid properties and sources from quartz-associated gold at the Betze-Post Carlin-type gold deposit, Nevada, United States. *Econ. Geol.* **2012**, *107*, 1351−1385.
(43) Götze, J.; Möckel, R.; Vennemann, T.; Müller, A. Origin and geochemistry of agates in Permian volcanic rocks of the Sub-Erzgebirge basin, Saxony (Germany). *Chem. Geol.* **2016**, *428*, 77−91.
(44) Baatartsogt, B.; Schwinn, G.; Wagner, T.; Taubald, H.; Beitter, T.; Markl, G. Contrasting paleofluid systems in the continental basement: a fluid inclusion and stable isotope study of hydrothermal vein mineralization, Schwarzwald district, Germany. *Geofluids* **2007**, *7*, 123−147.
(45) Götte, J.; Möckel, R.; Kempe, U.; Kapitonov, I.; Vennemann, T. Characteristics and origin of agates in sedimentary rocks from the Dryhead area, Montana, USA. *Mineral. Mag.* **2009**, *73*, 673−690.
(46) Matsuhisa, Y.; Goldsmith, J. R.; Clayton, R. N. Oxygen isotopic fractionation in the system quartz-albite-anorthite-water. *Geochim. Cosmochim. Acta* **1979**, *43*, 1131−1140.
(47) Götze, J.; Plötze, M.; Tichomirowa, M.; Fuchs, H.; Pilot, J. Aluminium in quartz as an indicator of the temperature of formation of agate. *Mineral. Mag.* **2001**, *65*, 407−413.
(48) Moxon, T. A re-examination of water in agate and its bearing on the agate genesis enigma. *Mineral. Mag.* **2017**, *81*, 1223−1244.
(49) Pfaff, K.; Romer, R. L.; Markl, G. U-Pb ages of ferberite, chalcedony, agate, 'U-mica' and pitchblende: constraints on the mineralization history of the Schwarzwald ore district. *Eur. J. Mineral.* **2009**, *21*, 817−836.
(50) Götze, J.; Tichomirowa, M.; Fuchs, H.; Pilot, J.; Sharp, Z. D. Geochemistry of agates: a trace element and stable isotope study. *Chem. Geol.* **2001**, *175*, 523−541.
(51) Götze, J.; Möckel, R.; Pan, Y. Mineralogy, Geochemistry and Genesis of Agate-A Review. *Minerals* **2020**, *10*, 1037.
(52) Gilg, H. A.; Morteani, G.; Kostitsyn, Y.; Preinfalk, C.; Gatter, I.; Strieder, A. J. Genesis of amethyst geodes in basaltic rocks of the Serra Geral Formation (Ametista do Sul, Rio Grande do Sul, Brazil): a fluid inclusion, REE, oxygen, carbon, and Sr isotope study on basalt, quartz, and calcite. *Miner. Deposita* **2003**, *38*, 1009−1025.
(53) Svetova, E. N.; Svetov, S. A. Agates from Paleoproterozoic Volcanic Rocks of the Onega Structure, Central Karelia. *Geol. Ore Deposits* **2020**, *62*, 669−681.
(54) Rodgers, K. A.; Cressey, G. The occurrence, detection and significance of moganite (SiO_2) among some silica sinters. *Mineral. Mag.* **2001**, *65*, 157−167.
(55) Richter, S.; Götze, J.; Niemeyer, H.; Möckel, R. Mineralogical investigations of agates from Cordón de Lila, Chile. *Andean Geol.* **2015**, *42*, 386−396.
(56) Williams, L. A.; Parks, G. A.; Crerar, D. A. Silica diagenesis, I. Solubility controls. *J. Sediment. Res.* **1985**, *55*, 301−311.
(57) Sigg, L.; Stumm, W. The interaction of anions and weak acids with the hydrous goethite (α-FeOOH) surface. *Colloids Surf.* **1981**, *2*, 101−117.
(58) Williams, L. A.; Crerar, D. A. Silica diagenesis, II. General mechanisms. *J. Sediment. Res.* **1985**, *55*, 312−321.
(59) Gaweł, B. A.; Ulvensøen, A.; Łukaszuk, K.; Muggerud, A. M. F.; Erbe, A. In situ high temperature spectroscopic study of liquid inclusions and hydroxyl groups in high purity natural quartz. *Miner. Eng.* **2021**, *174*, No. 107238.
(60) Howard, C. B.; Rabinovitch, A. A new model of agate geode formation based on a combination of morphological features and silica sol-gel experiments. *Eur. J. Mineral.* **2017**, *30*, 97−106.
(61) Chauviré, B.; Rondeau, B.; Mangold, N. Near infrared signature of opal and chalcedony as a proxy for their structure and formation conditions. *Eur. J. Mineral.* **2017**, *29*, 409−421.
(62) Chaklader, A. C. D. Effect of Trace Al_2O_3 on Transformation of Quartz to Cristobalite. *J. Am. Ceram. Soc.* **1961**, *44*, 175−180.
(63) Pisciotto, K. A. Diagenetic trends in the siliceous facies of the Monterey Shale in the Santa Maria region, California. *Sedimentology* **1981**, *28*, 547−571.

https://doi.org/10.1021/acsomega.2c02538
ACS Omega 2022, 7, 23858−23864